

Article

Associating Synoptic-Scale Weather Patterns with Aggregated Offshore Wind Power Production and Ramps

Bedassa R. Cheneka ^{1,*} , Simon J. Watson ¹  and Sukanta Basu ² 

¹ Wind Energy Section, Faculty of Aerospace Engineering, Delft University of Technology, 2629 HS Delft, The Netherlands; S.J.Watson@tudelft.nl

² Faculty of Civil Engineering and Geosciences, Delft University of Technology, 2628 CN Delft, The Netherlands; s.basu@tudelft.nl

* Correspondence: b.r.cheneka@tudelft.nl

Abstract: Large-scale weather patterns and their variability can influence both the amount of wind power production and its temporal variation, i.e., wind power ramps. In this study, we use a self-organizing map to cluster hourly sea level pressure into a discrete number of weather patterns. The dependency of wind power production and wind power ramps on these weather patterns is studied for the Belgian offshore wind farm fleet. A newly developed wavelet-surrogate ramp-detection algorithm is used for the identification of wind power ramps. It was observed that low-pressure systems, southwesterly and northeasterly wind flows are often associated with high levels of wind power production. Regarding wind power ramps, the type of transition between weather patterns was shown to determine whether ramp up or ramp down events would occur. Ramp up events tend to occur due to the transition from a high-pressure to a low-pressure system, or the weakening of the intensity of a deep low-pressure system. The reverse is associated with ramp down events.

Keywords: Belgian wind power; frequency of ramps; self-organizing maps; weather regimes



Citation: Cheneka, B.R.; Watson, S.J.; Sukanta, B. Associating Synoptic-Scale Weather Patterns with Aggregated Offshore Wind Power Production and Ramps. *Energies* **2021**, *14*, 3903. <https://doi.org/10.3390/en14133903>

Academic Editor: Eugen Rusu

Received: 17 May 2021
Accepted: 23 June 2021
Published: 29 June 2021

Publisher's Note: MDPI stays neutral with regard to jurisdictional claims in published maps and institutional affiliations.



Copyright: © 2021 by the authors. Licensee MDPI, Basel, Switzerland. This article is an open access article distributed under the terms and conditions of the Creative Commons Attribution (CC BY) license (<https://creativecommons.org/licenses/by/4.0/>).

1. Introduction

The total European wind power capacity reached 220 GW in 2020 [1]. During the same period, offshore wind power capacity also increased significantly from 4 GW to 25 GW. Furthermore, according to WindEurope's 'high scenario', up to 100 GW of wind power capacity could be installed offshore by 2030 [2]. This capacity of wind power will present new challenges for network operators seeking to balance supply and demand where a significant fraction of that supply comes from a non-dispatchable form of energy generation over a large area some distance from the load in many cases.

Wind speed and associated wind power ramps are influenced by both mesoscale and large-scale meteorological phenomena which cover a range of spatial and temporal scales [3–7]. Mesoscale systems develop over a time scale of hours which correspond to a spatial coverage of tens of kilometers (km) and include phenomena such as thunderstorms, land-sea breezes and cumulus convection. By contrast, large-scale synoptic systems comprise extra-tropical cyclones, troughs, ridges and frontal systems, cover hundreds of km and persist over timescales of several days.

It is well known that weather patterns influence the generation of wind power [8,9]. For instance, European wind power production shows a significant regional variation as a result of the prevailing weather patterns [10]. The occurrence of cyclonic regimes corresponds to an increase of wind power production across Northern Europe. Blocked (high-pressure) regimes lead to an increase of wind power production over southeastern Europe. By contrast, wind power production in the Mediterranean does not show a clear correlation with either cyclonic or blocked regimes. We believe that understanding the relationship between weather patterns and wind power generation helps in power system planning, energy trading and dispatch.

Studies have also demonstrated that the demand for electricity shows an association with weather patterns. For example, over the UK, low electricity demand days and high wind power capacity generation are associated with Icelandic low-pressure systems. However, high-electricity-demand days and low wind power capacity are related to high-pressure systems over Scandinavia and Great Britain [11]. Additionally, during prolonged cold spells, the Irish wind power capacity factors are low while the demand for electricity is relatively high [12]. These examples suggest that there are further benefits in classifying and quantifying the prevalence of different weather systems when balancing supply and demand where there is a large penetration of wind power.

Furthermore, weather patterns influence the magnitude and direction of large and rapid changes in wind power production known as wind power ramps. A study which looked at UK wind farms showed that the passage of cyclonic systems could cause wind power ramps over time scales of around four hours. However, the passage of frontal systems tends to produce short-duration power ramps of timescales in the range of 30–60 min [13]. Over Eastern Japan, the frequency of ramp up and ramp down events shows a strong association with particular weather patterns [14]. It was observed that ramp up events are mostly related to extra-tropical cyclones while ramp down events are primarily associated with reduced zonal (or meridional) gradients of the surface pressure.

The occurrence of power ramps tends to be associated with particular atmospheric circulations. Attempts have been made to group these circulations into a discrete number of weather patterns. The Lamb classification scheme is one of the earliest and most well-known approaches to classify large-scale European weather patterns focused over the British Isles [15]. The scheme initially consisted of only 10 weather patterns but was later extended to 26 [16]. A related classification scheme known as the GWL (Grosswetterlagen) scheme was developed using 29 weather patterns over Europe [17]. Recently, k-means clustering [18] and principal component analysis (PCA) [10] have been used to cluster European weather patterns into 30 and seven classes, respectively. The use of machine learning to classify weather patterns has increased in popularity in recent times. For example, a study showed the use of three different machine-learning techniques to identify extreme weather events in Taiwan [19] where they were shown to outperform more traditional objective weather classifiers. An alternative machine-learning approach to classify weather patterns is to use a self-organizing map (SOM). A SOM has advantages over other well-known clustering techniques. First, SOMs capture nonlinear patterns within the data that cannot be clustered using linear recognition tools such as PCA or Empirical Orthogonal Function (EOF) analysis. Furthermore, SOMs preserve the topological order of the weather patterns [20,21] leading to a smooth spatial transition from one weather pattern to the next. This is an advantage when grouping patterns into overarching circulation types, e.g., predominantly high or low pressure.

SOMs have been widely used in the field of atmospheric science to detect various trends, for example, to detect changes in atmospheric weather patterns due to climate change [22,23] and to quantify the connection between intra-seasonal rainfall variability and weather circulation [24]. They have also been used to identify the association of large-scale synoptic systems with extreme climate events [25–27], wind pattern classification [28] and wind power ramps [14]. In this paper, we classify large-scale European weather patterns and investigate how they affect the power output of offshore wind farms using the Belgian offshore fleet as an example.

2. Data

In this study, we use wind power data provided by the Belgian system operator, Elia [29] from the Belgian offshore wind farms located in the North Sea region at a longitude of between 2.7° and 3.0° E and a latitude of between 51.5° and 51.7° N. These sites were chosen because offshore wind power will make a significant contribution to future installed capacity, particularly in Northern Europe, and because the power production data are open access. The aggregated measured wind power is available from 2013 to date with a 15-min

resolution. In 2013, the aggregated rated power was 195 MW and by April 2020 had grown to 1608 MW. However, during 2015–2016, there was no change in rated power which was 712 MW. Thus, to simplify the analysis, in this study we consider only this two-year period. Furthermore, it was found that less than 1% of the data were missing for this period.

To cluster the weather patterns, we use sea level pressure (SLP) from the fifth generation of ECMWF's atmospheric reanalyses of the global climate (ERA5) [30] for the period 2003–2017. As the ERA5 data are of an hourly resolution, the 15-min wind power data are also aggregated hourly so that they can be directly associated with the meteorological data. Therefore, all wind power and ramp values in the following analysis are based on *hourly* values.

3. Methods

3.1. SOM Algorithm

The SOM was originally developed for pattern recognition [31–33] and is an unsupervised learning technique that maps high-dimensional input data onto a low-dimensional output space. In this paper, we wish to map an arbitrary pressure field to one of a finite number of classes to assess wind speed (and thus wind power) dependency on large-scale circulation patterns.

A SOM is a simple neural network that consists of an input layer. In our case, the input layer consists of hourly sea level pressure (SLP) for the period 2003–2017. This provides $n = 131,496$ temporal data samples on a regular spatial grid of $m = 201 \times 141 = 28,341$ values (Figure 1a). This input layer of n 1D data vectors (Figure 1b) is connected to a layer of i output neurons through a series of weight vectors (Figure 1c). The output layer is a 2D Kohonen map of 30 nodes where each node represents a series of representative weather patterns (Figure 1d) based on clustering of the input data.

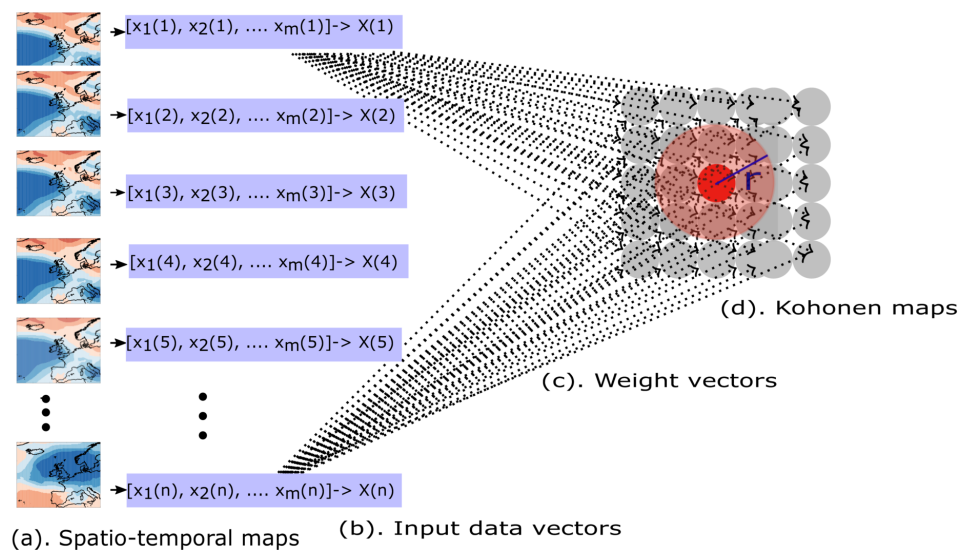


Figure 1. Schematic diagram of SOM: (a) n samples of hourly spatial SLP 2D maps containing m grid points (b) 2D spatial data converted into 1D vectors, (c) weight vectors (W_i) connecting input data with 2D Kohonen maps, (d) SOM topological maps and the neighborhood radius (σ). The red dot is a hypothetical Best-Matching Unit (BMU) which has the smallest Euclidean distance between the weight of the output neuron and the input data vector.

For simplicity, we initialize the weight vectors from a random sample of the input SLP data vectors. Linear initialization would provide faster convergence but is computationally expensive [31]. The SOM is trained over a series of iteration steps in this study using SOM_PAK software that uses a sequential SOM training algorithm [34]. At each step t , a Euclidean distance is used to calculate the distance between each 2D input data vector $X(t)$ and each of the i weight vectors $W_i(t)$. The output node whose weight vector, $W_c(t)$,

is closest to each input node is called the Best-Matching Unit (BMU) and has an index c given by:

$$c = \underset{i}{\operatorname{argmin}}(\|\mathbf{X}(t) - \mathbf{W}_i(t)\|) \quad (1)$$

Then, the weighting vectors of the BMU and those close by are updated to better reflect the input vector:

$$\mathbf{W}_i(t+1) = \mathbf{W}_i(t) + \alpha(t)h_{ci}(t)[\mathbf{X}(t) - \mathbf{W}_i(t)] \quad (2)$$

where $\alpha(t)$ is a learning rate which decreases monotonically as a function of iteration time, and h_{ci} is the Gaussian neighborhood function. The value of $\alpha(t)$ decreases linearly with iteration time:

$$\alpha(t) = \alpha_0 \left(1 - \frac{t}{t_{max}}\right) \quad (3)$$

where α_0 is the initial user defined learning rate, and t_{max} is the maximum iteration time.

The Gaussian neighborhood function is given by:

$$h_{ci}(t) = \exp\left(-\frac{\operatorname{sqdist}(c,i)}{2\sigma^2(t)}\right) \quad (4)$$

where the neighborhood radius size ($\sigma(t)$) also reduces linearly as a function of iteration t in a similar manner to $\alpha(t)$, and $\operatorname{sqdist}(c,i)$ is the squared geometric distance between the BMU and neuron i .

As the neurons are initialized randomly, two phases of training are required for the neurons to maintain a topological order. In the first, rough training phase, a relatively wide radius of influence ($\sigma_0 = 6$) is used, i.e., approximately the diameter of the Kohonen map (Figure 1d) and the initial learning rate, α_0 , is set to 0.05. In the second, fine-tuning phase, the training is iterated using a smaller radius ($\sigma_0 = 3$) and an initial learning rate of 0.02. Following [34], in the first phase σ_0 is about the size of the diameter of the map; and it is reduced to one third of it in the second phase.

In both training phases, the training passes through several iteration steps. In the rough training phase, the total number of iterations, t_{max} , is 10% of n (the number of input data vectors). In the fine-tuning phase, we use a Sammon mapping projection [35] at different iteration steps to check the topological order of the neurons to see if the SOM is sufficiently trained. If the Sammon projection shows a relatively 'twisted' neuron map (see Figure 2a) then the SOM is not fully trained whereas a more organized arrangement (Figure 2b) suggests that the SOM has been trained sufficiently.

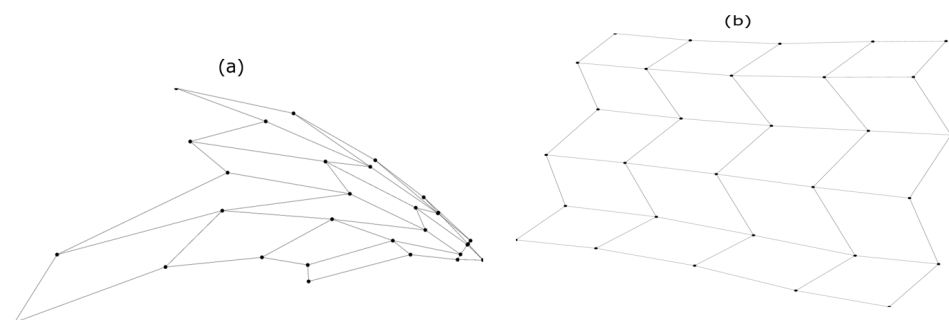


Figure 2. Sammon map projection of ERA5 hourly SLP during fine-tuning: (a) after 10,000 iteration steps, and (b) after 131,496 iteration steps.

3.2. Detecting Wind Power Ramps

This research involves the study of both mean power and rapid changes in offshore wind power, known as wind power ramps. To identify ramp events, we use the newly proposed wavelet-surrogate [36] algorithm. This method first generates a wavelet transform of an original time series. Additional wavelet transform is performed based on several random shuffles (100 times in this study) of the original power time series. The wavelet coefficients of this latter transform are used to discriminate the coefficients generated using the original time series from uncorrelated noise. Cheneka et al., 2020 [36] used a Daubechies level-1 (Haar) mother wavelet to generate the wavelet coefficients using 15-min aggregated wind power values up to a given maximum wavelet scale (a_{max}) and a discrimination level (W_T^*). Based on the hourly offshore wind power data, Figure 3 shows the application of the wavelet-surrogate (WS) algorithm to detect ramps using a value of $a_{max} = 20$ and four threshold values for W_T^* . As the discrimination level of W_T^* is reduced from 10% to 1%, the number and duration of detected ramps are reduced, i.e., a high percentage value of W_T^* will pick up a larger number of potentially weak ramps, whereas a smaller percentage value only picks up the strong ramps in a given time period. To provide a reasonable balance between these, we use a 5% discrimination level for W_T^* for the subsequent analysis. Please refer to Cheneka et al., 2020 [36] for further details.

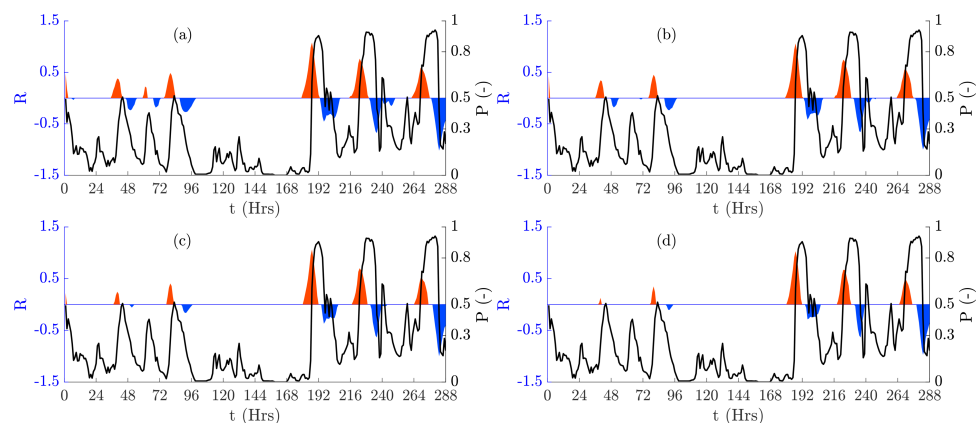


Figure 3. Detected normalized power ramps for the period of 20 to 31 May 2015 for $a_{max} = 20$ with discrimination levels, W_T^* of: (a) 10% (b) 5% (c) 2% and (d) 1%. Ramp-up events are shown in red and ramp-down events in blue.

4. Results

In this section, the main characteristics of the SOM-clustered weather patterns are first discussed. Then the dependence of the mean power production and power ramps on the different weather patterns are analyzed. Finally, some individual ramp case studies are analyzed in more detail. It should be noted that in all cases, results are normalized to the total rated capacity of the Belgian offshore wind farms during the period 2015–2016, i.e., 712 MW.

4.1. Weather Patterns

Based on the discussion in Section 1 concerning previous attempts to classify European weather patterns, we chose to classify the hourly ERA5 SLP for the period 2003–2017 into 30 weather patterns. The result is shown in Figure 4. Hereafter, we refer to these 30 patterns as SOM-based weather patterns. The figure highlights the advantage of using a SOM for classification as the weather patterns show a smooth transition from one weather pattern to the next. This allows the patterns to be grouped by climatology. For example, weather patterns at the center of the map (c2–e2 and c3–e3) show predominantly weak (slack) pressure gradients, especially over the North Sea, and are characteristic of the summer season [37]. The weather patterns at the right of the map (f1–f4) are dominated by blocked regimes/high pressure, which dominate the winter season [38].

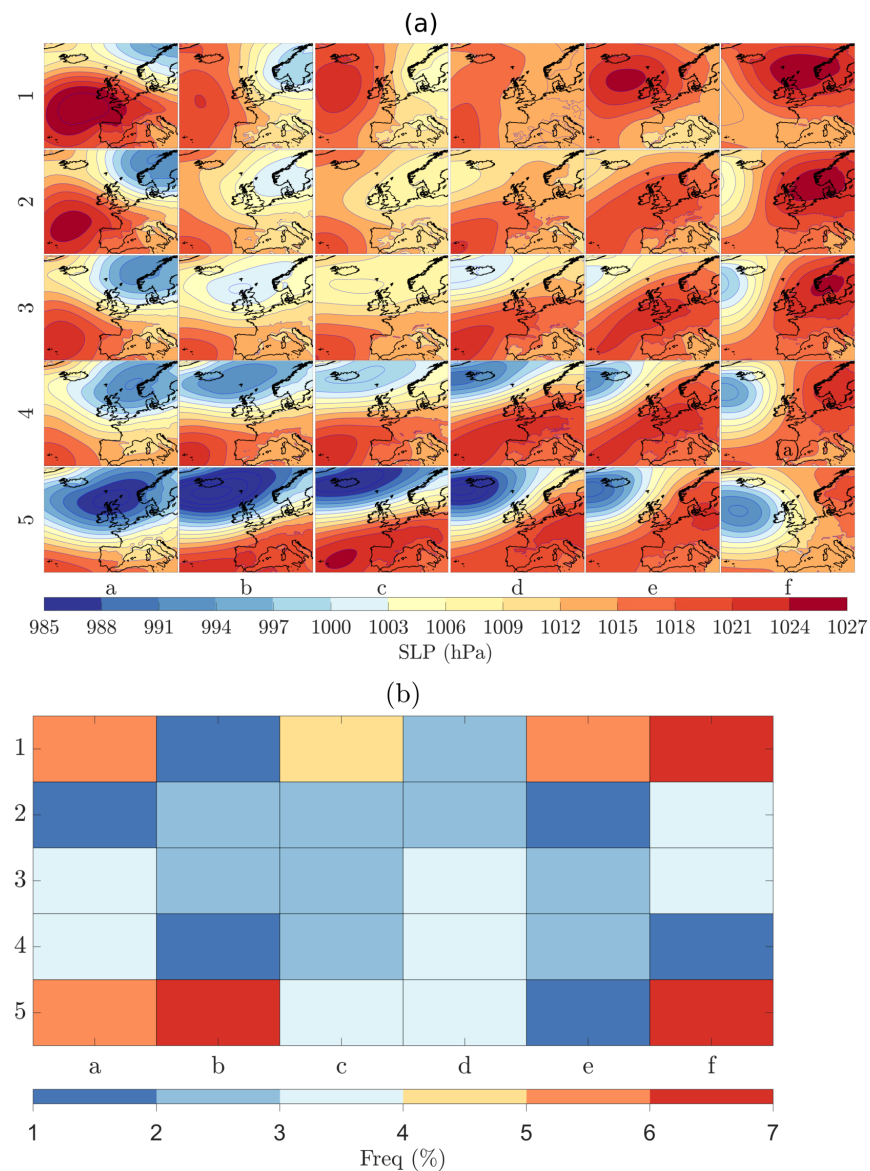


Figure 4. The SOM-based weather patterns using ERA5 hourly sea level pressure 2003–2017 and corresponding frequency of occurrence: (a) The SOM-based weather patterns. The color scale is hourly sea level pressure (SLP) in hPa and the contour lines are at intervals of 3 hPa; and (b) frequency of weather patterns in (%). Rows (1–5) and columns (a–f) are used to label the weather patterns.

When comparing the SOM-based weather patterns with those clustered using a PCA [10], we found that the SOM produces similar results [39]. It can be seen that the classification has captured the main European weather patterns including: Atlantic trough ($f4$, $f5$), Scandinavian trough ($a3$, $a4$), Atlantic ridge ($a1$, $a2$), Scandinavian blocking ($f1$), Greenland blocking ($e1$), Northerly flow ($b1$, $c1$) and British Isles Low Pressure ($a5$). The weather patterns at the bottom of the map are mainly dominated by zonal flow ($b5$ – $e5$). Moreover, we can see that the weather patterns which display strong pressure gradients are located at the edges of the map, i.e., right ($f1$ – $f4$): high pressure over Europe and Scandinavia, left ($a1$ – $a4$): high pressure over the Atlantic and low pressure over Scandinavia, top ($b1$ – $d3$): meridional flow and bottom ($a5$ – $f5$): low pressure and zonal flow. Those weather patterns in the center of the map show indistinct pressure systems with weak gradients. In Figure 4b, the frequency of the different weather patterns is shown. Notably, those weather patterns with distinct features at the edge of the map tend to occur more frequently. This likely reflects the fact that most pressure fields can be mapped to distinct weather patterns.

The SOM-based weather patterns are also compared with the Royal Netherlands Meteorological Institute (KNMI) synoptic charts to see how well synoptic systems at a particular point in time are captured using the six most frequently occurring patterns, i.e., *a1*, *e1*, *f1*, *a5*, *b5* and *f5*. The synoptic chart at 00:00 UTC associated with the first occurrence in the time series of each of these six weather patterns is used for validation. The resulting charts are shown in Figure 5.

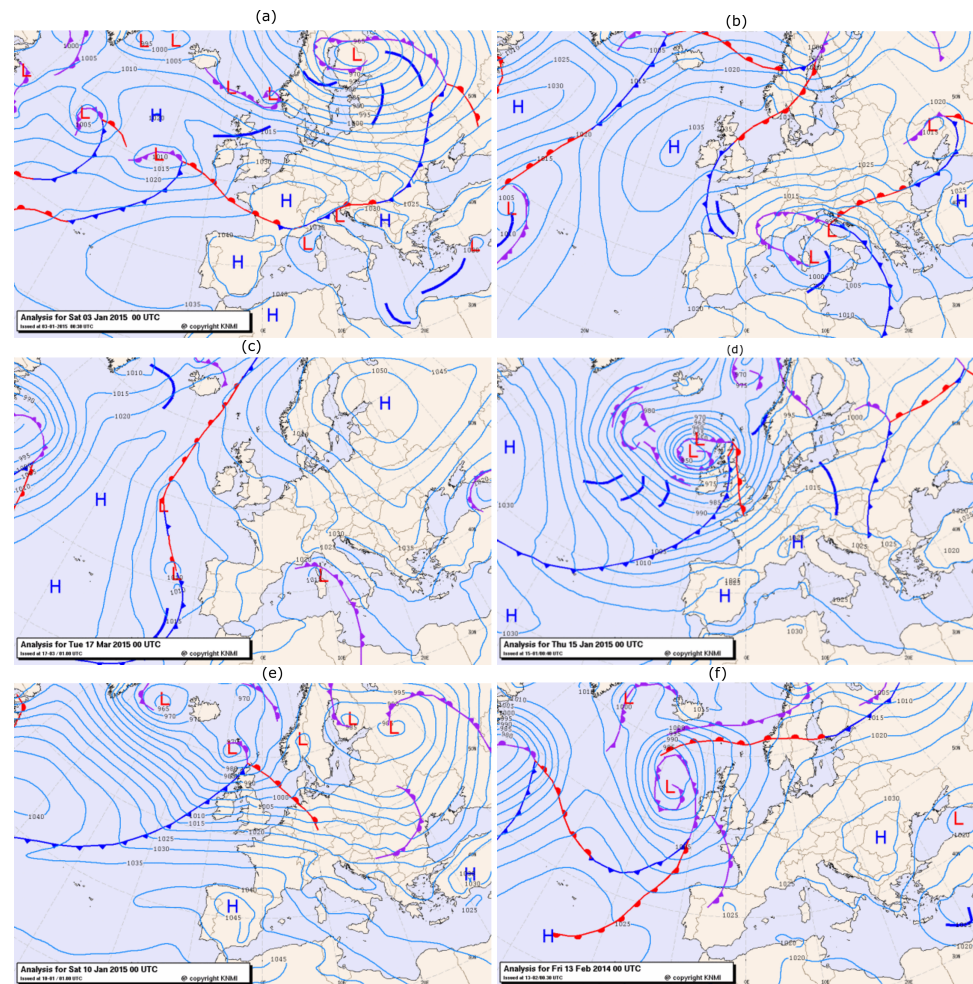


Figure 5. KNMI synoptic charts (<https://www.knmi.nl>, accessed on 5 May 2021) corresponding to the six most common SOM-based weather patterns at 00:00 UTC on: (a) 3 January 2015 (*a1*), (b) 6 February 2015 (*e1*), (c) 17 March 2015 (*f1*), (d) 15 January 2015 (*a5*), (e) 10 January 2015 (*b5*), and (f) 13 February 2015 (*f5*). The prominent synoptic features are shown: L (low pressure), H (high pressure), blue (cold front), red (warm front) and magenta (occluded front).

Even though the SOM-based weather patterns are based on the long-term period 2003–2017, in general, they capture quite well the individual synoptic systems on given days, with some slight differences. For example, on 3 January 2015, the low-pressure system centered over Finland and the extended high-pressure area west of the UK and south over continental Europe observed on the synoptic chart are essentially captured by weather pattern *a1*, though the small low to the west of the UK is not seen in the SOM-based weather pattern. The synoptic chart also shows a warm front to the southwest of the UK. The European (*e1*) and Scandinavian (*f1*) blocked regimes are clearly observed in the synoptic charts on 6 February 2015 (Figure 5b) and 17 March 2015 (Figure 5c), respectively. The synoptic chart on the 6 February 2015 also shows a warm front moving over the North Sea. Weather pattern *a5*, dominated by a low-pressure system over the UK is clearly visible in the synoptic chart of 15 January 2015 (Figure 5d) with cold and warm frontal systems

moving across the North Sea area. Figure 5e shows a zonal flow synoptic chart dominated by a southwesterly wind flow which is captured by weather pattern *b5*. This chart also shows a warm front over the North Sea region. Lastly, on 13 February 2015, the synoptic chart shows a low-pressure system over the Atlantic (Figure 5f) which is well captured by weather pattern *f5*. On this chart, frontal systems can be seen in the Atlantic with an occluded front approaching the English Channel.

In summary, the SOM-based clustering captures well the features of instantaneous weather systems and in many cases, frontal systems are likely to be observed which may lead to rapid changes in wind speed (wind power ramps).

4.2. Wind Power Trends by Weather Pattern

4.2.1. Wind Power Production

In Figure 6a, the frequency of normalized wind power production is shown by weather pattern. The highest values of power production that occur frequently are associated with those weather patterns located at the bottom left of the map shown in Figure 4 which are mainly characterized by zonal flow and cyclonic circulation (low-pressure systems), i.e., *a5*, *a4*, *a3*, *b5* and *b4*. However, frequent low-power production value is particularly associated with weather patterns where high pressure dominates, notably blocked regimes such as *f2* and *f3* and regimes in the center of the map with slack pressure gradients.

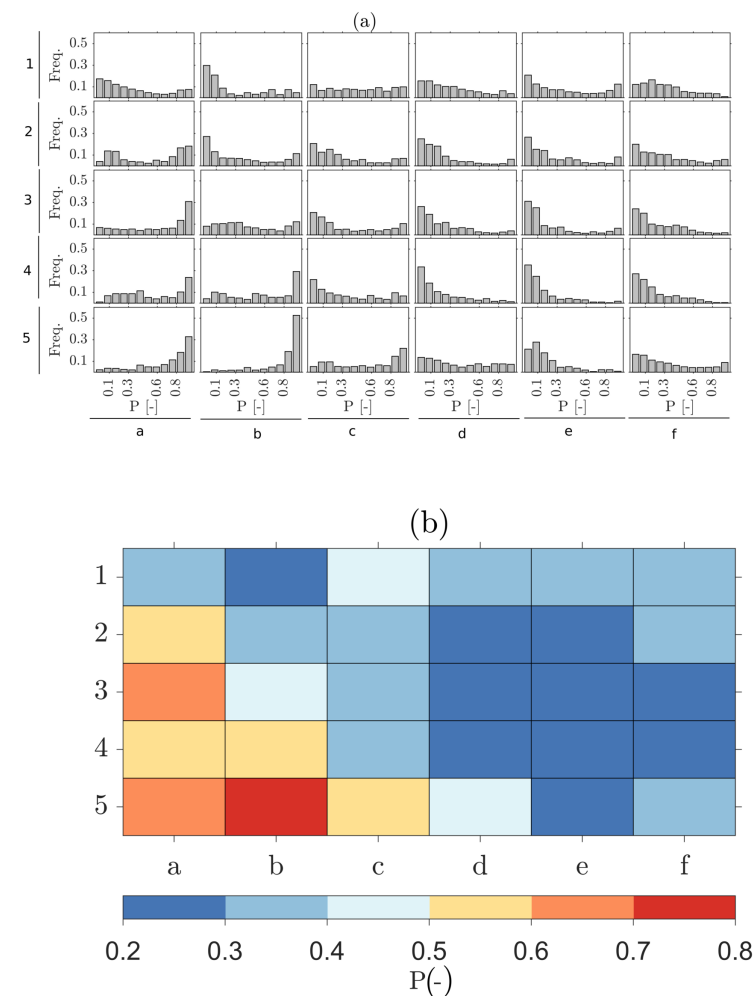


Figure 6. Normalized wind power production by weather patterns: (a) distribution of normalized wind power, and (b) mean value of normalized wind power (mean capacity factor).

In Figure 6b, the normalized mean wind power production by weather pattern is shown. This value can be considered to be the mean capacity factor of the combined offshore Belgian wind farm cluster. The overall mean capacity factor across all weather patterns is about 0.4. The values effectively summarize the distributions in Figure 6a but highlight the extreme differences in capacity factor across the different patterns ranging from 0.2 to 0.8. Maximum capacity is observed for the weather patterns mainly located at left-bottom which are characterized by cyclonic circulation systems. However, the weather patterns in the right are associated with low-capacity factor, and those weather patterns are mainly characterized by blocked regimes or high-pressure systems with a slack pressure gradient.

4.2.2. Wind Power Ramps

Figure 7 shows the frequency of wind power ramps by weather pattern which are detected using the wavelet-surrogate method with a 5% discrimination level for W_T^* and $a_{max} = 20$. These parameters can detect both short and long duration power ramps. The percentage of ramps is calculated based on the total number of power production values in each weather class (Figure 7a (ramp up) and Figure 7b (ramp down)); and as a fraction of the total number of ramps over the two-year period (Figure 7c (ramp up) and Figure 7d (ramp down)).

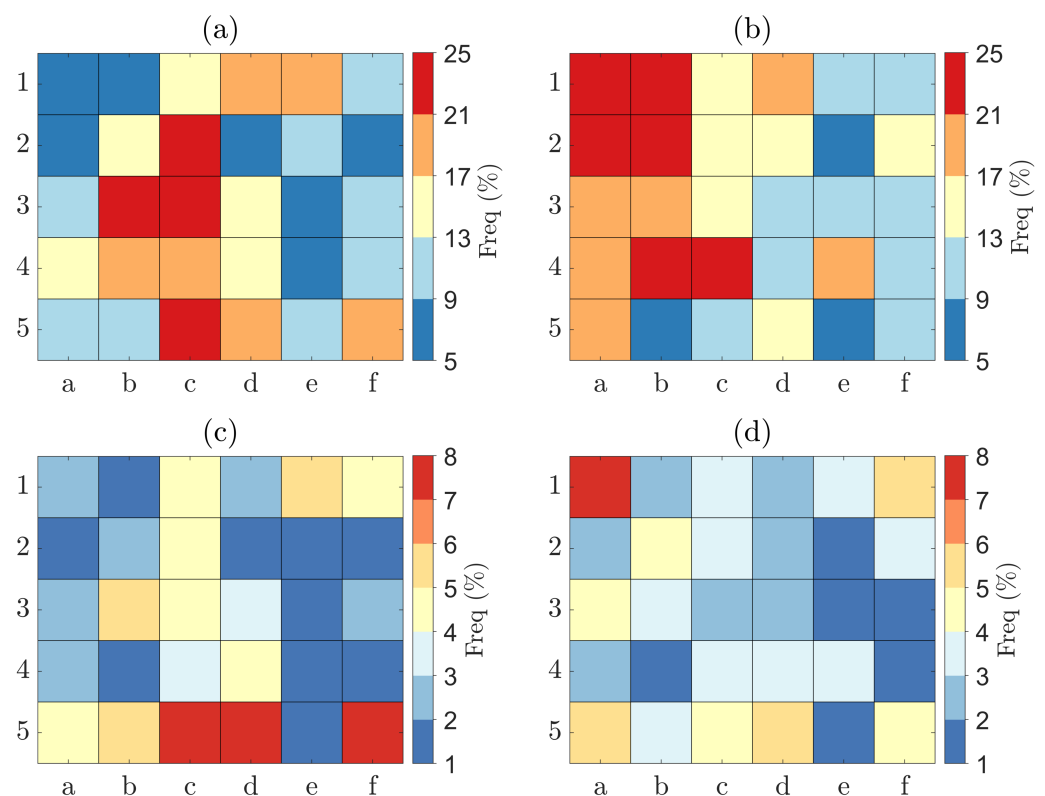


Figure 7. Frequency of ramp up and ramp down events as a function of weather pattern: (a) ramp up events as a fraction of the number of hours of generation classified as a particular pattern, (b) as (a) for ramp down events, (c) ramp up events as a fraction of the total number of ramps identified, and (d) as (c) for ramp down events.

In Figure 7a, it is seen that when weather patterns c2, b3, c3 and c5 are prevalent, the largest percentage of ramp up events occur. The first three of these patterns are associated with transitions from high to low-pressure systems when pressure gradients are relatively weak, but wind speeds are still sufficient to maintain a modest amount of

production. In such cases, wind turbines are operating below rated power in a steep part of the power curve and thus relatively small changes in wind speed can cause a large change in wind power. The high number of events in *c5* is less clear as there is a pattern of distinct westerly flow, though with modest winds when looking at the capacity factor values in Figure 6b. Again, this is likely to be associated with greater swings in production if operating frequently below rated power.

On the other hand, the largest percentage of ramp down events is seen when patterns *a1*, *a2*, *b1*, *b2* (in the top left of the SOM) and *b4* and *c4* (in the bottom left) prevail (see Figure 7b). There does not appear to be a clear link to the pattern of these circulations that could lead to a higher number of ramp down events, but again, the capacity factors are modest during these periods, so wind power output is likely to be variable for a similar reason as above.

When viewed as the percentage of the total number of ramps, the picture is slightly different. In this case, the most frequent number of ramp up events occurs during patterns *c5*, *d5* and *f5* (see Figure 7c). This is partly influenced by the frequency with which the synoptic situations fall within one of these patterns, but this is not the entire reason. Patterns *c5* and *d5* are not the most frequent patterns but show a proportionally higher number of ramp up events. The patterns *c5*, *d5* and *f5* are all associated with modest winds and again it is likely that the wind turbines will be operating in the below rated range. The ramp down events as a fraction of the total ramps show less variability (see Figure 7d), with the highest occurrence for pattern *a1* which was also seen in Figure 7a.

In summary, the occurrence of wind power ramps seems to be associated with modest wind speeds when wind turbines are operating at below rated power in the steepest part of the power curve. Another factor which could affect the prevalence of ramp events is the passage of fronts [40] which is not picked up from the pressure fields alone although the individual charts in Figure 5 shows that such activity is frequently present for several of the most commonly occurring patterns. Alternatively, the transition between particular patterns may play a role and this is explored in the next section.

4.2.3. Wind Power Ramp Case Studies

In this section, we look for temporal trends in weather-pattern transitions during ramp events, classifying the ramps into weak and strong wind power ramp cases as shown in Figures 8 and 9, respectively. In Table 1, the first four ramp cases, R1–R4 are relatively slowly evolving ramps (weak ramp rates), whereas the ramp cases, R5–R8 are stronger ramps that show a rapid increase or decrease over a relatively short period of time.

The temporal evolution of the weak ramp cases, R1–R4, along with the associated weather-pattern transitions just before, during and just after each ramp event are shown in Figure 8. The ramps are characterized by a significant rise or fall in power production over a long period. Figure 8a,c show ramp up events in green whereas Figure 8b,d show ramp down events in red. Figure 9 shows the equivalent results for the strong ramp cases R4–R8 where significant power changes are seen over a short period.

Table 1. Case study ramp start and end times (to the nearest hour) and type of ramp.

Ramp Cases	Start	End	Ramp Type
R1	26-November-2015 20:00	27-November-2015 15:00	ramp up
R2	22-November-2016 10:00	23-November-2016 01:00	ramp down
R3	23-January-2015 12:00	24-January-2015 02:00	ramp up
R4	09-March-2016 11:00	10-March-2016 01:00	ramp down
R5	19-May-2016 13:00	19-May-2016 23:00	ramp up
R6	04-February-2016 11:00	04-February-2016 20:00	ramp down
R7	27-May-2015 14:00	27-May-2015 22:00	ramp up
R8	09-May-2015 14:00	10-May-2015 02:00	ramp down

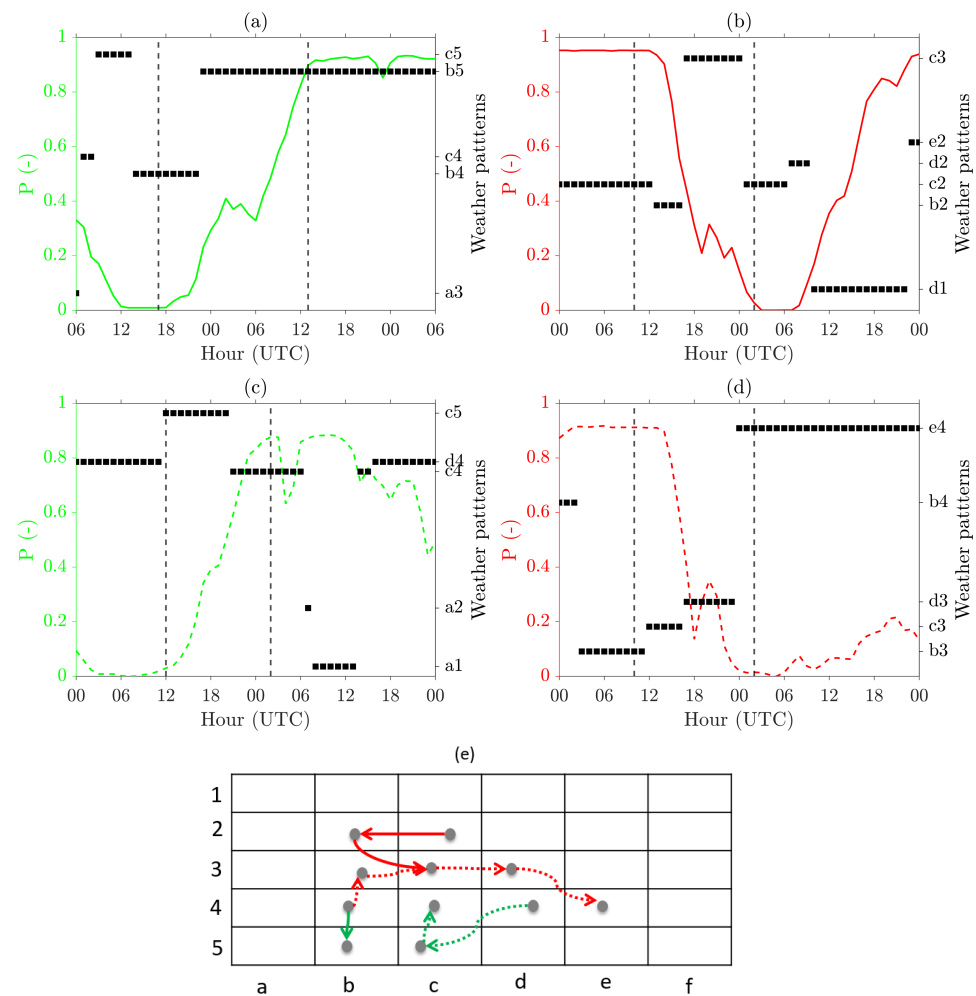


Figure 8. Weak wind power ramp cases and associated weather patterns: (a) R1 (b) R2 (c) R3 (d) R4, and (e) a sketch of the weather-pattern transitions for R1 (solid green line), R2 (solid red line), R3 (green dashed line) and R4 (red dashed line). R1–R4 periods are shown in Table 1. The vertical black dash lines in the (a–d) indicate the detected start and end time of the ramps.

By combining the temporal evolution of each ramp with the change in weather patterns observed it is possible to gain some insight into the cause of the ramp events. For example, for R1 (solid green line) and R3 (dashed green line), we can see that the start of the ramp up events are associated with a transition from weak low-pressure systems to strong low-pressure systems, i.e., *b4* to *b5* for R1 and *d4* to *c5* for R3. These weather patterns are located near the bottom of the SOM in Figure 4a. In these cases, the ramps are likely due to the fact that the wind turbine capacity factors increase as the low-pressure systems become deeper. The ramp down cases, R2 (solid red line) and R4 (dashed red line) are triggered when the low-pressure systems evolve to high-pressure systems. These weather patterns transition from the center left of the SOM to the right in these ramp cases. As a result of these weather-pattern transitions, the normalized wind power production decreases to almost to zero from near maximum capacity factors.

For the strong ramp cases in Figure 9, the first ramp up event, R5 (solid green line), occurs due to a transition from a weak low-pressure system (*c3*) to a strong low-pressure system accompanied by a southwesterly wind flow (*d4*). However, the second ramp up event, R7 (green dashed line), is triggered due to a transition from a weather pattern (*a1*) with a high-pressure system in the area of the wind farms transitioning to weak zonal/low pressure (*c3*). In this case, the normalized wind power production is close to zero during weather pattern *a1* as the high-pressure system leads to very low wind speeds around

turbine cut-in. The ramp down case, R6 (solid red line), occurs due to a transition from weather pattern *a1* to the weather pattern *d4* characterized by southwesterly wind flow. In this case, occluded and warm frontal systems contributed to the development of the ramp as seen in the KNMI synoptic chart (not shown). For the second ramp down event, R8 (red dashed line), a transition is seen from a weak pressure system (*d2*) to strong blocked regimes (*e3* and *f3*).

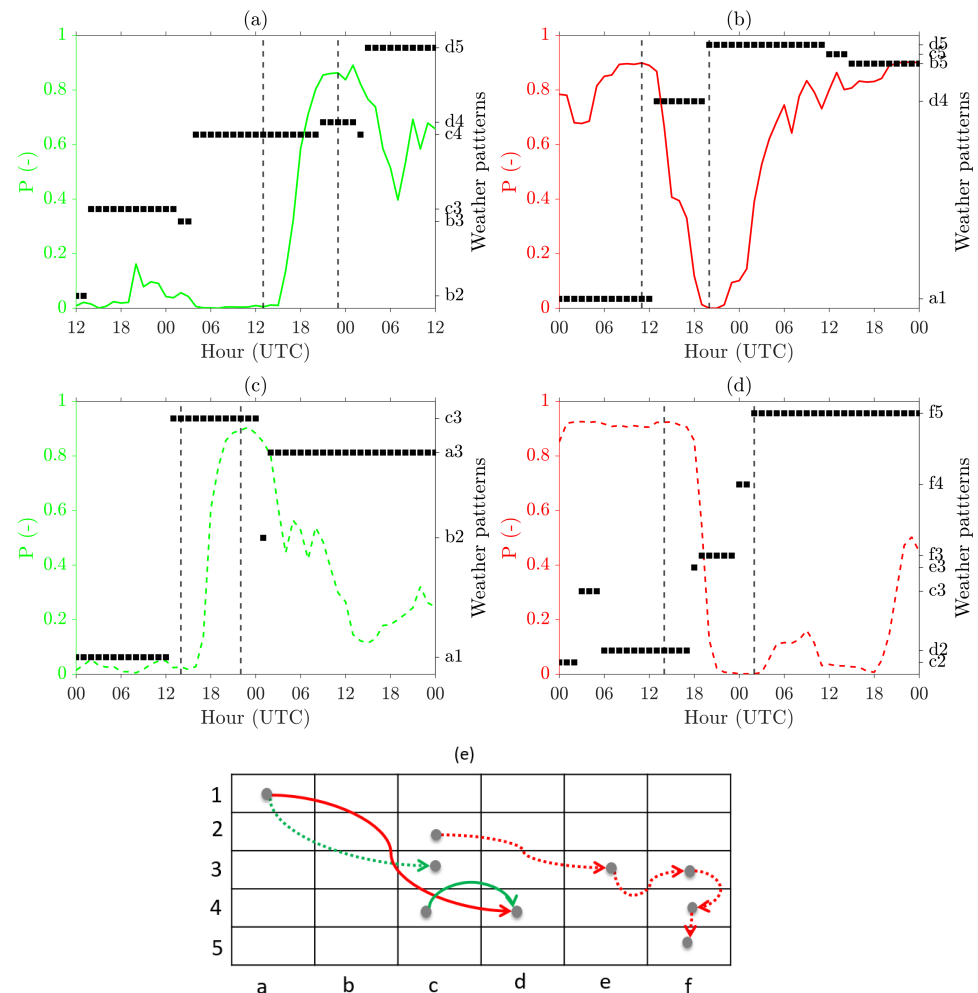


Figure 9. Strong wind power ramp cases and associated weather patterns: (a) R5 (b) R6 (c) R7 (d) R8, and (e) a sketch of the weather-pattern transitions for R5 (solid green line), R6 (solid red line), R7 (green dashed line) and R8 (red dashed line). R5–R8 periods are shown in Table 1. The vertical black dash lines in the (a–d) indicate the detected start and end time of the ramps.

It is worth noting that for the strong ramp events, the transitions seen in the SOM between weather patterns are larger compared to the weak ramps. This reflects the more rapid changes in wind speed associated with rapid changes in weather conditions and the fact that the data are hourly so that intermediate patterns are less likely to be resolved.

In summary, it can be seen that ramp events tend to be associated with a change in weather pattern. By studying the transition through different weather patterns, the type and strength of a ramp can be determined. The combination of weather-pattern transitions with information about frontal activity could enhance this still further. This would require a more detailed clustering approach using temperature information which is beyond the scope of this study.

5. Conclusions

In this study, we demonstrate the application of a SOM to classify weather patterns over the North Sea. The advantage of the SOM is shown in its ability to classify similar weather circulation patterns close together in the map allowing a higher-level overview of the prevailing weather systems.

The relationship between the clustered weather patterns and normalized wind power production for the Belgian offshore wind farm fleet has been quantified. Wind power production shows a maximum capacity factor for those weather patterns that are characterized by cyclonic (low-pressure) systems, northeasterly and zonal wind flow, whereas a weak pressure gradient and blocked regimes are the main cause for low-capacity factors.

Finally, we have studied the dependency of wind power ramps on prevailing weather patterns. In general, wind power ramps occur frequently for the weather patterns that are characterized by low-pressure systems, northeasterly and zonal wind flow. The type of weather-pattern transition determines the type of ramp. Eight ramp cases were studied to better understand the weather-pattern transitions which occurred during these events. It was seen that the ramp events were commonly associated with a change in weather pattern. For the four cases examined, ramp up events occurred during the transition from weak low-pressure systems to deep low-pressure systems. The four ramp down events were seen to be associated with a transition from low-pressure systems to blocked regimes.

For further work, it is recommended that additional information about the prevalence of frontal systems be included, for example, using a SOM to cluster spatial patterns in temperature. In addition, a more comprehensive analysis is required of the weather-pattern transitions that are seen for many ramp events to provide a deeper insight into the dependency of wind power ramps for different weather circulation patterns.

Author Contributions: B.R.C. analysed the data, generated the plots and wrote the first draft under the supervision of S.J.W. and S.B. Moreover, S.J.W. and S.B. edited the manuscript. All authors have read and agreed to the published version of the manuscript.

Funding: This research received no external funding.

Institutional Review Board Statement: Not applicable.

Informed Consent Statement: Not applicable.

Data Availability Statement: The hourly sea level pressure data from ERA5 which are used in this study to identify the weather patterns are available in the public domain. In addition, the Belgian offshore wind power production data are provided freely by Elia (<https://www.elia.be/>).

Conflicts of Interest: The authors declare no conflict of interest.

References

1. WindEurope. *2020 Statistics and the Outlook for 2021–2025*; Published in February 2021; WindEurope: Brussels, Belgium, 2021.
2. WindEurope. *Wind Energy in Europe: Scenarios for 2030*; WindEurope: Brussels, Belgium, 2017.
3. Orlanski, I. A rational subdivision of scales for atmospheric processes. *Bull. Am. Meteorol. Soc.* **1975**, *56*, 527–530.
4. Fujita, T.T. Tornadoes and downbursts in the context of generalized planetary scales. *J. Atmos. Sci.* **1981**, *38*, 1511–1534. [[CrossRef](#)]
5. Fujita, T. Mesoscale classifications: Their history and their application to forecasting. In *Mesoscale Meteorology and Forecasting*; Springer: Berlin/Heisenberg, Germany, 1986; pp. 18–35.
6. Emanuel, K.A. Overview and definition of mesoscale meteorology. In *Mesoscale Meteorology and Forecasting*; Springer: Berlin, Germany, 1986; pp. 1–17.
7. Thunis, P.; Bornstein, R. Hierarchy of mesoscale flow assumptions and equations. *J. Atmos. Sci.* **1996**, *53*, 380–397. [[CrossRef](#)]
8. Brayshaw, D.J.; Troccoli, A.; Fordham, R.; Methven, J. The impact of large scale atmospheric circulation patterns on wind power generation and its potential predictability: A case study over the UK. *Renew. Energy* **2011**, *36*, 2087–2096. [[CrossRef](#)]
9. Correia, J.; Bastos, A.; Brito, M.; Trigo, R. The influence of the main large-scale circulation patterns on wind power production in Portugal. *Renew. Energy* **2017**, *102*, 214–223. [[CrossRef](#)]
10. Grams, C.M.; Beerli, R.; Pfenninger, S.; Staffell, I.; Wernli, H. Balancing Europe’s wind power output through spatial deployment informed by weather regimes. *Nat. Clim. Chang.* **2017**, *7*, 557–562. [[CrossRef](#)] [[PubMed](#)]

11. Thornton, H.E.; Scaife, A.A.; Hoskins, B.J.; Brayshaw, D.J. The relationship between wind power, electricity demand and winter weather patterns in Great Britain. *Environ. Res. Lett.* **2017**, *12*, 064017. [CrossRef]
12. Cradden, L.C.; McDermott, F. A weather regime characterisation of Irish wind generation and electricity demand in winters 2009–11. *Environ. Res. Lett.* **2018**, *13*, 054022. [CrossRef]
13. Drew, D.R.; Barlow, J.F.; Coker, P.J. Identifying and characterising large ramps in power output of offshore wind farms. *Renew. Energy* **2018**, *127*, 195–203. [CrossRef]
14. Ohba, M.; Kadokura, S.; Nohara, D. Impacts of synoptic circulation patterns on wind power ramp events in East Japan. *Renew. Energy* **2016**, *96*, 591–602. [CrossRef]
15. Lamb, H.H. British Isles weather types and a register of the daily sequence of circulation patterns 1861–1971. *Geophys. Mem.* **1972**, *116*.
16. Jenkinson, A.; Collison, F. An initial climatology of gales over the North sea. Synoptic Climatology Branch Memorandum. *Meteorol. Off.* **1977**, 1–62.
17. Gerstengarbe, F.; Werner, P. *Katalog der Grosswetterlagen Europas Nach Paul Hess und Helmut Brezowski 1881–1992*; Deutscher Wetterdienst: Offenbach, Germany, 1993.
18. Neal, R.; Fereday, D.; Crocker, R.; Comer, R.E. A flexible approach to defining weather patterns and their application in weather forecasting over Europe. *Meteorol. Appl.* **2016**, *23*, 389–400. [CrossRef]
19. Su, S.H.; Chu, J.L.; Yo, T.S.; Lin, L.Y. Identification of synoptic weather types over Taiwan area with multiple classifiers. *Atmos. Sci. Lett.* **2018**, *19*, e861. [CrossRef]
20. Liu, Y. Patterns of ocean current variability on the West Florida Shelf using the self-organizing map. *J. Geophys. Res.* **2005**, *110*. [CrossRef]
21. Liu, Y.; Weisberg, R.H.; Mooers, C.N.K. Performance evaluation of the self-organizing map for feature extraction. *J. Geophys. Res.* **2006**, *111*. [CrossRef]
22. Horton, D.E.; Johnson, N.C.; Singh, D.; Swain, D.L.; Rajaratnam, B.; Diffenbaugh, N.S. Contribution of changes in atmospheric circulation patterns to extreme temperature trends. *Nature* **2015**, *522*, 465–469. [CrossRef]
23. Francis, J.; Skific, N. Evidence linking rapid Arctic warming to mid-latitude weather patterns. *Philos. Trans. R. Soc. Math. Phys. Eng. Sci.* **2015**, *373*, 20140170. [CrossRef] [PubMed]
24. Oettli, P.; Tozuka, T.; Izumo, T.; Engelbrecht, F.A.; Yamagata, T. The self-organizing map, a new approach to apprehend the Madden-Julian Oscillation influence on the intraseasonal variability of rainfall in the southern African region. *Clim. Dyn.* **2013**, *43*, 1557–1573. [CrossRef]
25. Cavazos, T. Using Self-Organizing maps to investigate extreme climate events: An application to wintertime precipitation in the Balkans. *J. Clim.* **2000**, *13*, 1718–1732. [CrossRef]
26. Gibson, P.B.; Perkins-Kirkpatrick, S.E.; Uotila, P.; Pepler, A.S.; Alexander, L.V. On the use of self-organizing maps for studying climate extremes. *J. Geophys. Res. Atmos.* **2017**, *122*, 3891–3903. [CrossRef]
27. Loikith, P.C.; Lintner, B.R.; Sweeney, A. Characterizing large-scale meteorological patterns and associated temperature and precipitation extremes over the Northwestern United States using self-organizing maps. *J. Clim.* **2017**, *30*, 2829–2847. [CrossRef]
28. Durán, P.; Basu, S.; Meißner, C.; Adaramola, M.S. Automated classification of simulated wind field patterns from multiphysics ensemble forecasts. *Wind Energy* **2020**, *23*, 898–914. [CrossRef]
29. Marsboom, P.J. Belgian Wind Forecasting-Phase 1. *Elia Publ.* **2012**, *13*, 25.
30. Hersbach, H.; Bell, B.; Berrisford, P.; Biavati, G.; Horányi, A.; Muñoz Sabater, J.; Nicolas, J.; Peubey, C.; Radu, R.; Rozum, I.; et al. ERA5 Hourly Data on Single Levels from 1979 to Present. Copernicus Climate Change Service (C3S) Climate Data Store (CDS). 2018. Available online: <https://cds.climate.copernicus.eu> (accessed on 5 December 2020).
31. Kohonen, T.; Schroeder, M.R.; Huang, T.S. (Eds.) *Self-Organizing Maps*, 3rd ed.; Springer: Berlin/Heidelberg, Germany, 2001.
32. Kohonen, T. The self-organizing map. *Proc. IEEE* **1990**, *78*, 1464–1480. [CrossRef]
33. Kohonen, T. Essentials of the self-organizing map. *Neural Netw.* **2013**, *37*, 52–65. [CrossRef] [PubMed]
34. Kohonen, T.; Hynninen, J.; Kangas, J.; Laaksonen, J. Som pak: The self-organizing map program package. *Rep. A31 Hels. Univ. Technol. Lab. Comput. Inf. Sci.* **1996**, *1*, 39–40.
35. Sammon, J.W. A nonlinear mapping for data structure analysis. *IEEE Trans. Comput.* **1969**, *100*, 401–409. [CrossRef]
36. Cheneka, B.R.; Watson, S.J.; Basu, S. A simple methodology to detect and quantify wind power ramps. *Wind Energy Sci.* **2020**, *5*, 1731–1741. [CrossRef]
37. Cortesi, N.; Torralba, V.; González-Reviriego, N.; Soret, A.; Doblas-Reyes, F.J. Characterization of European wind speed variability using weather regimes. *Clim. Dyn.* **2019**, *53*, 4961–4976. [CrossRef]
38. van der Wiel, K.; Bloomfield, H.C.; Lee, R.W.; Stoop, L.P.; Blackport, R.; Screen, J.A.; Selten, F.M. The influence of weather regimes on European renewable energy production and demand. *Environ. Res. Lett.* **2019**, *14*, 094010. [CrossRef]
39. Cheneka, B.R.; Watson, S.J.; Basu, S. The impact of weather patterns on offshore wind power production. In *Journal of Physics: Conference Series*; IOP Publishing: Bristol, UK, 2020; Volume 1618, p. 062032.
40. Pichault, M.; Vincent, C.; Skidmore, G.; Monty, J. Characterisation of intra-hourly wind power ramps at the wind farm scale and associated processes. *Wind Energy Sci.* **2021**, *6*, 131–147. [CrossRef]